Improving Millimeter Radar Attenuation Corrections in High-Latitude Mixed-Phase Clouds via Radio Soundings and a Suite of Active and Passive Instruments

Petros Kalogeras⬡ and Alessandro Battaglia⬡

Abstract—**Supercooled liquid clouds are very frequent in high-latitude regions. In addition to their substantial effect on visible and infrared radiation, they affect the signal of millimeter radars by producing nonnegligible attenuation. Such attenuation must be properly corrected if the information of millimeter radars is used in quantitative retrievals for inferring ice microphysical properties. This study proposes a multisensor scheme for refining the vertical distribution of supercooled liquid water content (SLWC) compared to state-of-the-art methods that equipartition the liquid water path measured by microwave radiometer to all pixels identified as cloudy by the radars and warmer than −40 °C. Our methodology is applicable in high-latitude, mixed-phase environments based on the synergy between radar and lidar binary cloud phase masking, microwave radiometer, and radio sounding observations. The technique is demonstrated via data collected by the U.S. Department of Energy (DoE) Atmospheric Radiation Measurement (ARM) Program climate research facility at the North Slope of Alaska (NSA) and compared with the state-of-the-art methods. Path integrated attenuation (PIA) at W- and G-band frequencies (>95 GHz) is then assessed. Results indicate that the different in-cloud distributions of the liquid condensate lead to round-trip PIA discrepancies of cloudy volumes that range in [2, 5] dB at W- and G-band frequencies. These differences far exceed those encountered when changing some of the algorithm's arbitrary assumptions and weighting functions.**

Index Terms—**Attenuation measurement, clouds, electromagnetics for remote sensing, lidar data, radar data.**

I. INTRODUCTION

IN THE past 30 years, millimeter-wavelength radars have played a paramount role in atmospheric cloud research by providing a better understanding of clouds and precipitation

and their feedbacks in the Earth's climate system [1]. Radars in the Ka (frequencies between 26.5 and 40 GHz) and W (75–110 GHz) bands, mainly with transmitter frequency close to 35 (8 mm) and 94 GHz (3-mm wavelength), have been deployed in ground-based [2], airborne, and spaceborne [3] configurations since the last decade of 20th century. Boosted by advancements in radar technology, novel radars with frequencies in the next higher band (110–300 GHz), the so-called G-band, are now a reality, e.g., with the Vapor In-Cloud Profiling Radar (VIPR) system developed at JPL already in operation [4], [5] and with other systems currently under development. Due to their improved sensitivity to smaller particles, these radars have been proposed for a variety of cloud microphysics applications when operated in synergy with lower frequency cloud radars [5]–[7] and for profiling water vapor when designed with multiple tones within a water vapor absorption line [8]–[10].

The obvious drawback when moving up in frequencies is associated with the attenuation of the different atmospheric components: gases and hydrometeors [11]. The focus of this study is on high-latitude clouds generated in cold and dry environment below freezing temperatures, characterized by persistent mixed-phase clouds [12]. In such conditions, we can exclude the presence of liquid precipitation, which is generally an important source of attenuation even at the lower frequencies [13], while wavebands up to 40 GHz can be practically considered not attenuated, and radiation at frequencies close to 100 GHz and above may still suffer nonnegligible attenuation caused by atmospheric gases, supercooled liquid droplets, and ice (rimed) crystals [14]. Any quantitative estimate associated with cloud and precipitation requires upfront an attenuation correction that recovers the effective reflectivity of the backscattering volume under examination.

Effective reflectivities can then be used to estimate extensive cloud microphysical properties such as ice water content (IWC) or snow rate in single-frequency approaches (e.g., [15]) or can be exploited in multifrequency techniques to derive information on particle size [16] or ice-growth processes (aggregation/accretion, as demonstrated in [17]). Recent studies [5], [18]–[24] have underlined the potential of dual- and triple-frequency measurements across X-, Ku-, Ka-, W-, and G-bands in the characterization of ice cloud

microphysics; however, in all studies, attenuation corrections at the higher frequencies are imperative in order to consistently compare measured and simulated values and thus properly interpret the data.

Radar attenuation corrections are generally stabilized by integral constraints that can be derived in correspondence to natural targets of known reflectivity (surfaces) or known differential reflectivity (e.g., by using the fact that Rayleigh scatterers at the cloud top should yield the same effective reflectivity [25]) and/or by additional measurements (e.g., passive microwave radiometers can provide estimates of liquid water path (LWP) [26]). While gas attenuation can be sensibly distributed along the radar path according to the vertical distribution of temperature, pressure, and water vapor, the presence of supercooled liquid water (SLW) layers remains elusive when only radar observations are considered. In the first order, one approach is to distribute the LWP equally across the radar-detected cloud thickness, only excluding regions colder than $-40\,°C$ (e.g., [17], [20]).

Traditionally, estimates of liquid cloud locations are based on lidar/ceilometer measurements that provide accurate and precise measurements of cloud-base heights [27]. Nevertheless, lidar-based observations alone often fail to generate liquid water detection profiles for the entire cloud depth because these sensors attenuate sharply when encountering intervening liquid-bearing cloudy volumes. Other methods based on three-channel microwave radiometers, including one channel in the W-band [28], can provide estimates of the temperature of the cloud liquid but are troublesome in the presence of multilayered SLW clouds. A recent analysis in [29] has showcased an additional (Ka-band) radar-only cloud phase partitioning that can reliably distinguish liquid bearing from ice-only volumes. The method is particularly effective for liquid located in the cloud-top regions and only uses radar Doppler moments. Ka-band radars never fully attenuate in high-latitude subfreezing temperature clouds.

The scope of this work is to describe an improved millimeter radar attenuation correction scheme for high-latitude mixed-phase clouds. The technique is applicable to all ground-based cloud supersites (such as those of the Atmospheric Radiation Measurement (ARM) and the Cloud-Net programs [30], [31]), which in addition to the millimeter radars typically host lidars/ceilometers, passive microwave radiometers, and routinely launch balloon soundings. The methodology is based on an optimal combination of all these instruments in the characterization of the vertical profile of gases and supercooled liquid layers. This enables a more realistic liquid partitioning of the total LWP retrieved by the passive microwave radiometer in the column sensed by the radars.

Section II introduces the dataset and observing systems employed in this study. Section III provides a recapitulation of radar signal attenuation mechanisms, followed by the algorithm description of the proposed attenuation correction scheme (Section IV). A characteristic case study involving a high-latitude, mixed-phase scene is presented in Section V. Section VI outlines a sensitivity analysis in relation to implemented components of the technique in Section IV. The main discussion points of the study are summarized in Section VII.

TABLE I
ARM NSA.KaZR System Main Characteristics in Correspondence to the Two Operating Modes: Chirp (MD) and Burst (GE)

FACILITY	NSA (C1)	
OPERATING MODE	KaZR.MD	KaZR.GE
LATITUDE (°N)	71.32	
LONGITUDE (°E)	−156.61	
ANTENNA AMSL (m)	7	
FREQUENCY (GHz)	34.89	34.83
PRF (Hz)	2771	
PULSE WIDTH (ns)	3967	300
DWELL TIME (s)	3.7	
GATE SPACING (m)	29.98	
LOWER BOUND (m)	695	108
UPPER BOUND (m)	17484	17526

II. Dataset and Observing Systems

High-latitude mixed-phase clouds are the focus of this study. All utilized data are obtained by the U.S. Department of Energy (DoE) Atmospheric Radiation Measurement (ARM) Program climate research facility at Barrow, Alaska [North Slope of Alaska (NSA) (C1)] [32]. Utilized sensors are: 1) the zenith pointing Ka-band ARM cloud radar (KaZR) [33]; 2) the high spectral resolution lidar (HSRL) [34] (lidar data are available at hsrl.ssec.wisc.edu); 3) the microwave water radiometer (MWR); and 4) radio sounding deployments launched every 6–12 h.

From the KaZR chirp mode, follow a radar-only, binary cloud phase partitioning (based on [29]) that segregates ice/liquid volumes. This cloud phase mask is reliable in detecting SLW at cloud tops and is applied at cloudy volumes when the lidar signal is no longer available due to extinction by either liquid water or optically thicker ice. The HSRL is a 532-nm, depolarization lidar from which system another binary mask is independently derived; the HSRL cloud phase mask (based on [27]) segregates cloud volumes into four phases (clear, aerosol, ice, and liquid) and serves as the benchmark solution for all lidar-detected volumes. Radio sounding measurements are used in evaluating the atmospheric gas attenuation. Relative humidity with respect to liquid (S_{liq}) is used as an indicator of the likelihood of liquid water clouds. The liquid relative humidity is reserved for in-cloud, radar-detected volumes when the lidar is not available due to signal extinction. MWRs offer retrieved, path-integrated liquid water amounts (LWP) [26], which provide a constraint to the methodology presented in Section IV.

The Ka-band radar operates in two modes: chirp (MD) and burst (GE). Although the radar-based cloud phase mask applies only the KaZR.MD mode, the burst is additionally incorporated because, as shown in Table I, the vertical depth of the radar blind zone at near-antenna ranges is much reduced for the burst (100 m) as opposed to chirp (700 m). Thereby, burst mode reflectivities are merged with the chirp, thus significantly expanding the available radar-based observations in proximity of the radar antenna. Data coregistration is carried out via linear interpolations in time and range with 3.7 s and 30-m resolution, respectively. The radio soundings are coregistered via a temporally weighted average scheme that

applies at least the two recent most deployments, which are never more than 12 h apart.

III. MILLIMETER RADAR ATTENUATION CORRECTION

The cumulative effect of absorption and scattering (i.e., extinction or attenuation) due to atmospheric propagation in active observing systems is attributed to three factors, attenuation due to atmospheric gases, liquid condensate, and/or frozen particulates. The radar reflectivity factor $z(r; \lambda)$ (in mm^6 m^{-3}) at a given wavelength λ and range r can be [35], [36]

$$z(r; \lambda) = z_e(r; \lambda) \exp\left[-2\int_{r_\circ}^{r}\left(\sum_j \gamma(\xi; \lambda)_j + \gamma(\xi; \lambda)_{\text{LWC}}\right.\right.$$
$$\left.\left. + \gamma(\xi; \lambda)_{\text{IWC}}\right)d\xi\right] \quad (1)$$

where z_e is the effective (i.e., nonattenuated) reflectivity at the same range, $\gamma(\xi; \lambda)_j$ is the attenuation coefficient (i.e., extinction cross section per unit volume, in m^{-1}) of the jth gaseous species, and $\gamma(\xi; \lambda)_{\text{LWC}}$ and $\gamma(\xi; \lambda)_{\text{IWC}}$ are the attenuation coefficients for liquid water content and IWC, respectively.

The conversion to logarithmic units (dB) follows by application of the $10\log_{10}$ operator on both sides of (1). The resulting equation is

$$Z(r; \lambda) = Z_e(r; \lambda) - 2\int_{r_\circ}^{r}\left[\sum_j K(\xi; \lambda)_j + \alpha(\lambda)_{\text{LWC}}\text{LWC}(\xi)\right.$$
$$\left. + \alpha(\lambda)_{\text{IWC}}IWC(\xi)\right]d\xi \quad (2)$$

where uppercase Z (or Z_e) is the radar reflectivity factor (in dBZ), $K(\xi; \lambda)_j = 10\log_{10}(e)\,\kappa(\xi; \lambda)_j$ is the logarithmic absorption coefficient (in dB km^{-1}) per molecular species (in which case molecular absorption is assumed much larger than their scattering in incident Ka-to-W wavebands), and $\alpha(\lambda)_{\text{LWC}}$ and $\alpha(\lambda)_{\text{IWC}}$ are the specific attenuation coefficients (in dB km^{-1} (kg m^{-3})$^{-1}$) for liquid and ice, with LWC(ξ) and IWC(ξ) the liquid- and ice-water contents (in kg m^{-3}), respectively. The extinction optical depth (or thickness) is defined as

$$\int_{r_\circ}^{r}\gamma(\xi; \lambda)d\xi \equiv \tau_e(r; r_\circ, \lambda) \quad (3)$$

and the attenuation correction equation becomes

$$Z_e(r; \lambda) = Z(r; \lambda) + 2\times(\text{PIA}(r; \lambda)_{\text{GAS}} + \text{PIA}(r; \lambda)_{\text{LWC}}$$
$$ + \text{PIA}(r; \lambda)_{\text{IWC}}) \quad (4)$$

with $\text{PIA}(r; \lambda) \equiv 10\log_{10}(e)\times\tau(r; \lambda)$ (in dB) the one-way path integrated attenuation (PIA; experience by the radar up to range r, for each atmospheric constituent separately). Equation (4) relates the measured reflectivity Z with the effective Z_e given the cumulative effect of all extinction events along the optical path. Uncertainties related to the PIA can

be significant to DWR-based ice microphysical studies that rely—in part—on operating frequencies greater than 40 GHz.

The gaseous attenuation is treated in [37] via sounding-based information (of ambient temperature, total atmospheric, and water vapor pressures). The PIA due to ice can be estimated via extinction–reflectivity relations [25], [38]. The PIA due to liquid clouds requires a sensible distribution of the liquid water content along the column, which may follow from the three-sensor technique described hereafter.

IV. LWC VERTICAL DISTRIBUTION

The scheme for the distribution of the MWR-retrieved LWP along any vertical profile is based on a three-sensor synergy by utilization of: 1) HSRL; 2) KaZR (pulse compression mode and chirp); and 3) radio soundings. The per-sensor applied fields are: 1) binary HSRL cloud phase mask [27]; 2) binary radar-based cloud phase mask [29] restricted only to cloud top; and 3) interpolated (via temporal-weighted averages) relative humidities with respect to liquid. The MWR-retrieved LWP [26] constrains the total amount of liquid water per profile of observations.

The HSRL is filtered by its quality flag mask that determines at what altitude the lidar fully attenuates. In-cloud data points are defined by the radar-based criterion SNR ≥ -10 dB, while extrapolated dry-bulb temperatures (via temporal-weighted averages) constrain mixed-phase atmospheric domains, given $T_{\text{dry}} \in [-40, 0]$ °C. Liquid relative humidity is retained only for data points that are seen as in-cloud by the radar and the lidar has already fully attenuated. Across all observational scenarios, as long as the lidar signal remains available, the applied phase partitioning is the lidar-based alone. This is driven by the confidence that the depolarization lidar is the most reliable SLW estimator, and thus, this sensor always supersedes the other two.

Since the lidar signal (at 532 nm) is more susceptible to complete extinction than the Ka-band radar (at 8.6 mm), the radar may detect clouds at ranges greater than the lidar when the latter has fully attenuated at lower altitudes due to optically thick liquid water or ice. In this case, the algorithm applies either the radar-based cloud phase mask or S_{liq}. Specifically, assuming that H_R is the maximum range at which the radar signal remains available (for SNR ≥ -10 dB) and similarly H_L for the lidar (based on the quality flag mask), then if $|H_R - H_L| \geq 300$ m or $H_L - H_R > 300$ m, the radar mask is not applied; conversely, if $H_R - H_L > 300$ m, the radar mask is utilized.

On a per-profile basis, the case corresponding to the detection of only minute LWP amounts (<20 g m^{-2}) is not considered at all because PIAs even at G-band frequencies will be less than 0.2 dB (one way). This figure corresponds to the minimum detectable quantity for the passive microwave radiometer as well. If the LWP exceeds 20 g m^{-2}, then all the liquid-bearing volumes that the lidar signal penetrates (as seen by the lidar phase mask) will receive 20 g m^{-2}, where this value is equipartitioned among those volumes. The remainder of the LWP, i.e., (LWP $-$ 20) g m^{-2}, is then allocated to the observing systems as follows: 90% is apportioned to the
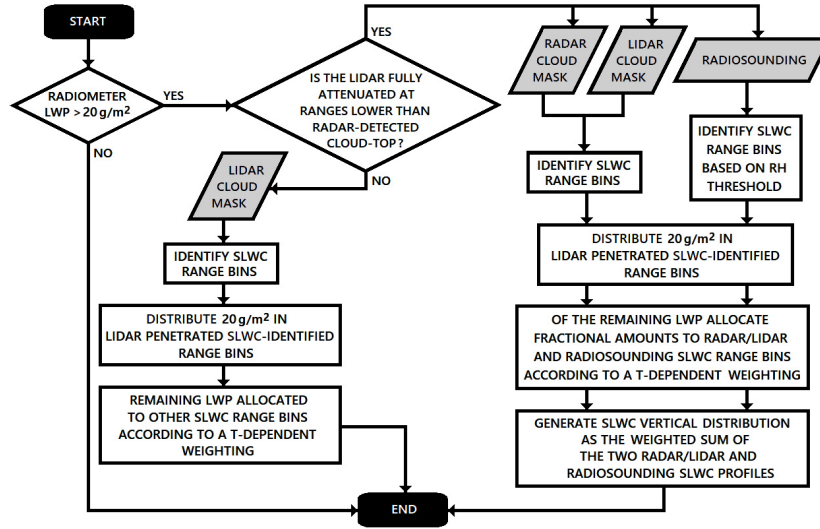
Fig. 1. Flowchart for mapping the LWC vertical distribution based on the synergy between Doppler radar, depolarization lidar, MW radiometer, and radio soundings (further description in the text).

SLW-detected range bins as seen by both radar and lidar binary cloud phase masks (of whatever possible combination, i.e., lidar-only, radar-only, or by both systems combined) and the remaining 10% is allocated to the liquid relative humidity range bins for which $S_{liq} > 0.85$.

The amount of liquid water content $LWC(r_j)$ (in g m^{-3}), at each applicable range bin, is thus given by

$$LWC_{R/L}(r_j) = \frac{1}{\Delta r} \ f(T(r_j)) \times (0.9 \ (LWP - 20)) \quad (5)$$

$$LWC_{RS}(r_j) = \frac{1}{\Delta r} \ f(T(r_j)) \times (0.1 \ (LWP - 20)) \quad (6)$$

where r_j is the range bin in which SLW is allocated, Δr is the gate spacing (constant, 30 m), and $f(T(r_j))$ is a weight based on the dry-bulb temperature at the given range according to the linear function: $g(T) = (1/40)T + 1$, $T \in [-40, 0]$ °C. This scheme is applied for all observational scenarios for which it is LWP > 20 g m^{-2}.

The applied scheme relies on a temperature-based weighting that allocates greater amounts of LWC to range bins of warmer ambient temperatures. As hinted by earlier studies [39]–[41], the suggestion is that atmospheric regimes of elevated temperatures also seem to sustain greater amounts of liquid condensate aloft. In an effort to corroborate such findings, we have analyzed MWR-based LWP products at the site of Barrow, for the period 2014–2019. Fig. 2, in particular, offers certain insights on the LWP occurrence frequency variation with ambient temperature, specific to the Alaskan, mixed-phase observational scenes. This figure showcases the LWP statistical occurrence at different surface temperatures and clearly demonstrates that as the temperature lessens, so does the total amount of the atmospheric liquid water in the radiometer's line of sight. It should be mentioned that Fig. 2 utilizes temperature information only at the ground (virtually at sea level in the case of Barrow), and thus, any atmospheric inversions aloft are not ascertainable. Although there is no direct comparison between LWP and LWC, Fig. 2 supports the idea of a higher likelihood
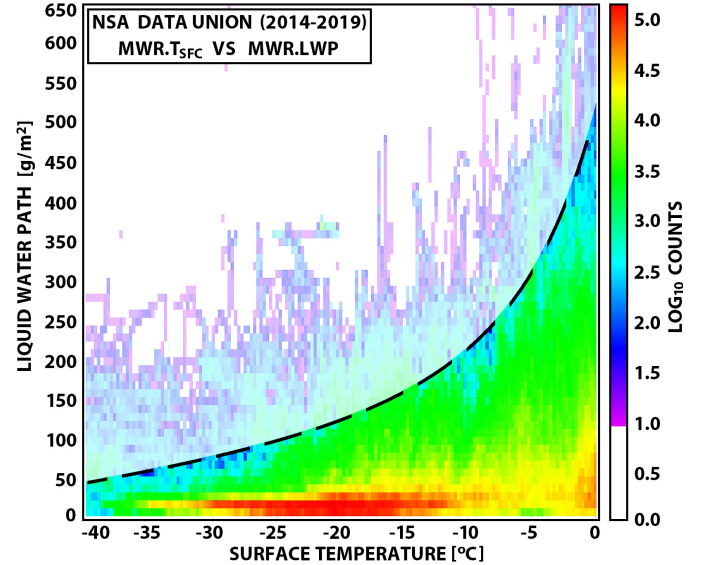

Fig. 2. Density scatter plot relating the MWR-retrieved path integrated liquid water amount (LWP) against the surface temperature at the site of Barrow (NSA, C1), for the period January 2014–May 2019. Only snapshots of below-freezing-point ambient temperatures (at ground level) are considered. The dashed line segregates roughly the 95% percentile of the LWP occurrence frequency at 5° temperature intervals.

of larger LWC occurring at warmer ambient temperatures. Nevertheless, any analogy between temperature and LWC remains highly uncertain, and thus, it can only be meaningful statistically. To that end, a sensitivity analysis that follows in Section VI allows for a broad envelope of possibilities for such T-LWC relations, thereby highlighting the impact of the temperature-based weighting on both the resulting LWC and attenuation profiles.

Regarding the fixed amount of 20 g/m^2 out of the total available LWP that is allocated to range bins of thin super-cooled liquid water content (SLWC) layers that the lidar signal penetrates, this can be estimated qualitatively by the

formula $LWP = (2/3) \times \tau \times r_e$, which is applicable in the geometric optics regime (i.e., assuming validity of the extinction paradox). In this relation, the LWP is given in g/m², τ is the optical depth, and r_e is the effective radius of a water droplet, in μm. For supercooled clouds of $r_e = 10$ μm, the choice for $LWP = 20$ g/m² corresponds to an optical depth of 3 (and larger for smaller r_e). The resulting round-trip transmissivity will thus be in the order of $\exp(-6) = 2.5 \times 10^{-3}$, amounting to a 99.75% signal loss of an attenuation -26 dB between the high reflectivity of the SLW targets and the HSRL minimum detectable signal. Still, with a typical dynamic range of 50–70 dB, even such attenuation amounts are not sufficient to fully extinguish the lidar, in which case signal returns may still be recorded. The assumed value will roughly sit between optical thicknesses producing no extinction and full extinction of the lidar signal and is deemed appropriate for the scope of the study. In fact, small changes to this value will not alter the attenuation correction since the corresponding LWP is comparable with the radiometer uncertainty.

V. CASE STUDY

A case study with peculiar features is here presented. The depicted case highlights a scene from the Barrow site on October 28, 2017. This event consists of an upper layer cold cloud with cloud base at a near-constant altitude of 5 km (AMSL) and low-level hydrometeor formations extending up to 1 km (AMSL) until 1000 UTC, as shown in the reflectivity panel [Fig. 3(a)]. The reflectivity field showcased here follows from the merging of the two transmitting modes (the chirp and burst modes, indicated by KaZR.MD and KaZR.GE, respectively) in order to optimize sensitivity and signal at closer ranges, in view of the two modes' blind zone depths (see Table I). Thereby, the reflectivity defines all data points registered as in-cloud based on the radar detection threshold of SNR ≥ -10 dB.

Fig. 3(b) shows the HSRL cloud phase mask in which five classes are presented for clear, aerosol, ice, and liquid; the latter has been additionally segregated into optically thick or thin (tenuous) when the lidar signal is not fully attenuated and optically thick clouds otherwise. The lidar is prone to extinction due to either liquid water or optically thicker ice of larger extinction coefficients, although this scene highlights a mostly attenuated HSRL at near-ground ranges due to a persistent SLW presence throughout.

Fig. 3(c) shows the binary radar-based cloud phase mask that is characterized by its two classes, "SLW" or "otherwise" (aerosol/ice). For visual clarity, the coloring of this mask is presented such that magenta/green corresponds to the liquid/ice radar-demarcated pixels in which the lidar signal remains available or orange/gray corresponds to the same partition when the lidar has fully attenuated at lower ranges. Data points for $Z_{Ka} \notin [-32, +8]$ dBZ fall outside of the radar-based phase partition algorithm's applicability [29]; those pixels are outlined by the blue color.

It is in multilayered events such as the one presented here that the relevance of the radar-based mask comes to the forefront. The highest likelihood of SLWC presence is identified

by the depolarization lidar if and when that remains available. Otherwise, the detection of any SLW-bearing volumes is relegated to the Doppler radar's capability for doing so. According to Fig. 3(b) and (c) for this event, the utilization of the HSRL cloud phase mask is significantly hampered due to the sensor's full extinction at the lowest altitudes. Yet, Fig. 3(c) reveals additional cloud phase-property insights based on the radar spectral widths and reflectivity vertical gradients; the absence of Doppler spectra with spectral width larger than 0.15 m s⁻¹ in conjunction with reflectivity gradients less than 5 dB km⁻¹ strongly points to the absence of SLW therein [29]. On the other hand, the radar-based mask suggests a higher probability for SLW at around 1.8 and 2.3 km (AMSL), past 1000 UTC, which is in-part corroborated by intermittent intervals of lidar availability, discernible in Fig. 3(b). Furthermore, cloud-top, liquid-bearing volumes usually appear with a vertical depth of about 200 m, based on high-latitude, mixed-phase conditions climatological analyses [29].

Low-level liquid (e.g., haze) is generally not detectable by the radar mask due to blind zone depth or radar dynamic range limitations. This fraction of the liquid condensate, observed here at ranges less than 1 km (AMSL) for the full scene duration, is well demarcated by the lidar. The radar-based phase partitioning [Fig. 3(c)] is entirely chirp-dependent due to the enhanced sensitivity of this mode in better detecting cloud-top domains, yet starts from 700 m (AMSL) (see Table I). This cloud mask is effective only at cloud-top regimes.

Fig. 3(d) shows the extrapolated liquid relative humidity (S_{liq}), filtered by data points classified as in-cloud to the merged radar signal (SNR ≥ -10 dB), where the lidar is fully attenuated. The filtering is adopted because LWC is only allocated in regions with radar-detected clouds and where the lidar signal is not available anymore due to full extinction. The relative humidity with respect to liquid, albeit a weaker constraint, is one additional factor utilized in estimating the presence of SLW when $S_{liq} > 0.85$.

Fig. 3(e) shows the extrapolated dry-bulb temperature (T_{dry}). The current scene demonstrates below-freezing-point environmental conditions for its entire duration, given that ambient temperatures do not exceed -5 °C. The temperature falls below -40 °C at about 6 km (AMSL), above which ranges only ice clouds may be encountered. Finally, the time series of Fig. 3(f) demonstrates the MWR-retrieved LWP of nonnegligible values in the range between 80 and 350 g/m⁻². Conclusively, the portrayed scene illustrates significant amounts of optically thicker SLW at near-surface levels and another ice-only cloud layer [>4.5 km (AMSL)] that is well detected by the radar but completely missed by the lidar, due to full attenuation within the thick low SLW layer.

Fig. 4(a) shows the LWC vertical distribution (in a $\log_{10}$ scale) if this were to be equipartitioned across all in-cloud radar-detected volumes of $T_{dry} \in [-40, 0]$ °C, without the application of any weighting function (this is the technique currently proposed by several authors). Conversely, Fig. 4(b) shows the vertical distribution of the LWC based on our procedure (Section IV), with obvious differences compared to the equipartition method. Prior to 1000 UTC, Fig. 4(b) shows that all the LWCs are allocated in volumes of the low-level
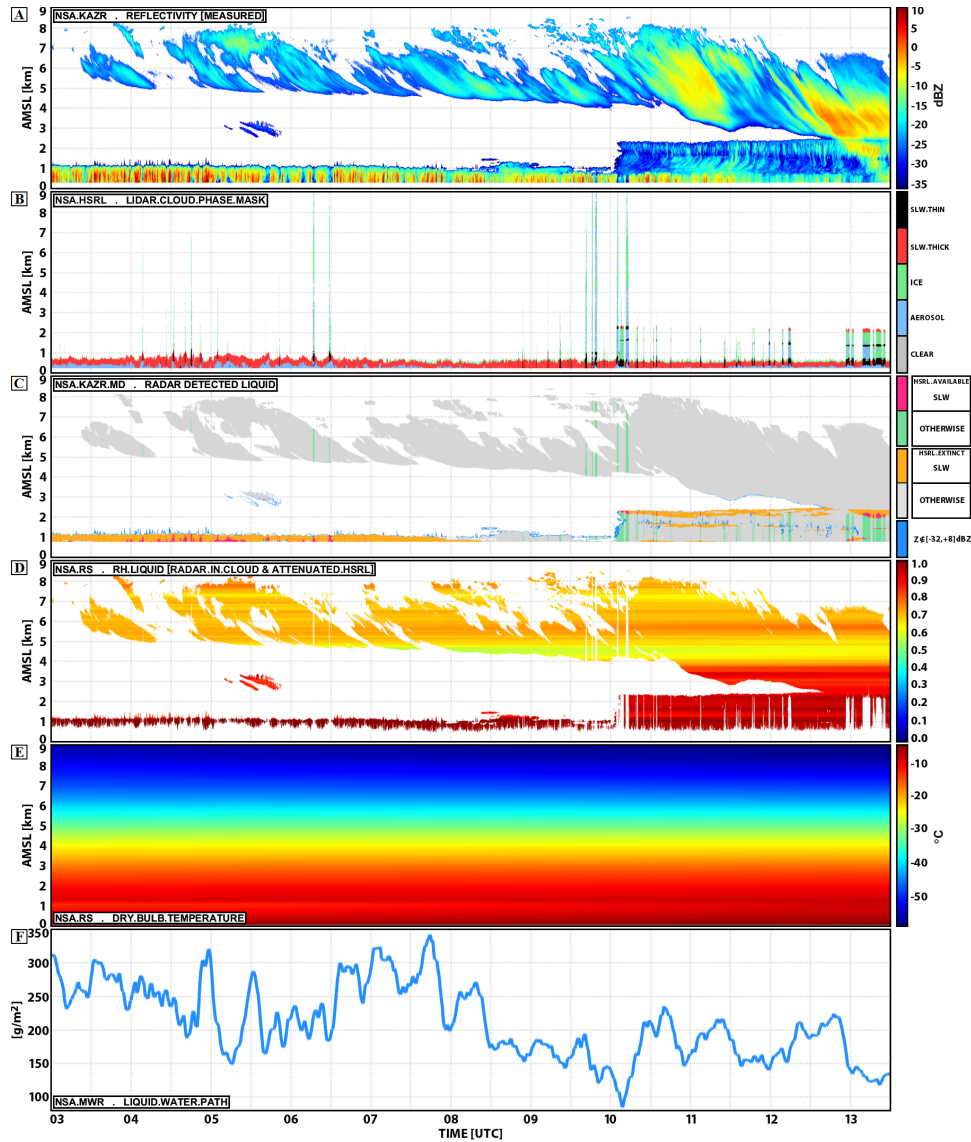
Fig. 3. Time–height plots of an NSA case on October 28, 2017, during 03:00–13:30 UTC, 0–9 km (AMSL), for the fields: (a) radar reflectivity factor (merged chirp and burst modes), (b) HSRL cloud phase mask, (c) radar-based cloud phase mask, (d) in-cloud liquid relative humidity (SNR ≥ −10 dB for an attenuated lidar), (e) dry-bulb temperature, and (f) MWR-retrieved LWP time series.
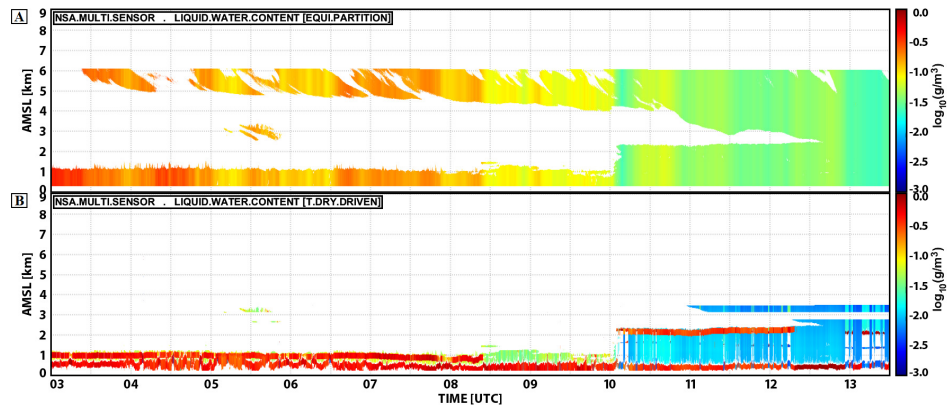

Fig. 4. Time–height plots of the scene shown in Fig. 3 of the estimated liquid water content fields based on (a) equipartition for in-cloud, radar-detected data points of $T_{dry} \in [-40, 0]$ °C and (b) three-sensor synergy of Section IV.

cloud [<1 km (AMSL)]. This is attributed to the radar-based cloud mask that does not point to the presence of SLW in the upper level cloudy volumes, given the lidar unavailability

throughout. After 1000 UTC, Fig. 4(b) shows how most of the LWC is allocated in volumes at either near-ground altitudes [<0.5 km (AMSL)], based on the lidar signal, or at about
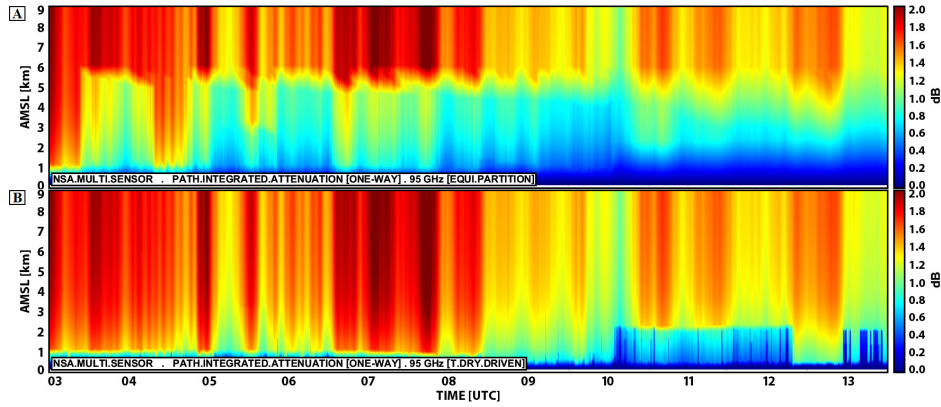
Fig. 5. Time–height plots of the scene shown in Fig. 3 of the one-way PIA at 95 GHz. (a) Exhibits the PIA that corresponds to the LWC vertical distributions highlighted in Fig. 4(a). (b) Similarly for the PIA of the LWC vertical distribution of Fig. 4(b).
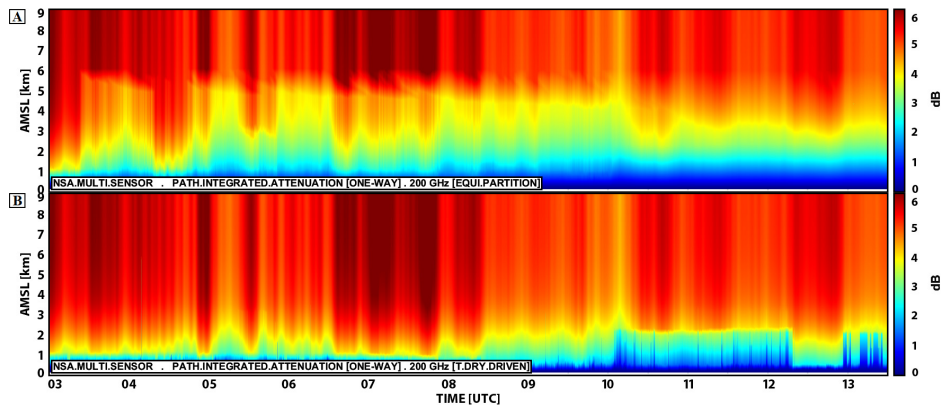

Fig. 6. Time–height plots of the scene shown in Fig. 3 of the one-way PIA at 200 GHz. (a) Exhibits the PIA that corresponds to the LWC vertical distributions highlighted in Fig. 4(a). (b) Similarly for the PIA of the LWC vertical distribution of Fig. 4(b).

2 km (AMSL), pertaining to the cloud-top radar-detected SLW, as shown in Fig. 3(c). For all other in-cloud, lidar-extinct pixels of $S_{liq} > 0.85$, our algorithm allows for a marginal additional LWC allocation still, yet the LWC distribution is predominantly determined by the combined radar/lidar binary masks that receive 90% of the LWP.

Figs. 5 and 6(a) and (b) show the one-way PIAs that follow from the application mentioned in [37] at 95 and 200 GHz, respectively, when the applied LWCs are of the equipartition or the three-sensor methodology in Section IV. The current context considers only W-to-G-band frequencies because, only at those higher frequencies, absorption optical depths due to SLW become markedly significant. The optical depths are evaluated by accounting the extrapolated fields of: 1) total atmospheric pressure; 2) water vapor partial pressure; 3) dry-bulb temperature; and 4) a distribution of the liquid condensate (LWC). The one-way PIAs are evaluated by $PIA_\lambda = 10 \log_{10}(e) \times (\tau_a)_\lambda$, where $(\tau_a)_\lambda$ is the spectrally dependent absorption optical depth. For ranges farther away from the radar, the PIAs converge toward the same numbers in both cases: at 95 GHz for up to 2 dB and 200 GHz around 6 dB. An evident PIA discrepancy between the two PIA profiles is manifested particularly at lower altitudes. Clearly, the greater the LWC assigned to closer-to-the-ground ranges,

the faster the PIA reaches its upper end values for any given snapshot. For the equipartitioned LWC distribution, PIA_λ gradually increases as long as there exist in-cloud data points and reaches its maximum only past the upper most altitude of the radar-detected cloudy volumes. For the three-sensor LWC distribution technique, more pronounced PIA_λ amounts are reached at lower altitudes. As a result, PIA discrepancies become relevant closer to the radar antenna, more so at G-band frequencies.

Fig. 7 shows an example of the profile at 11:20:02 UTC, 0.0–6.5 km (AMSL). Fig. 7(a) (reflectivity) in conjunction with Fig. 7(b) (dry-bulb temperature) shows in-cloud, radar-detected range bins of $[-40, 0]$ °C. Fig. 7(c) shows the equipartitioned LWC profiles based on the adopted filtering, i.e., SNR ≥ -10 dB $\wedge$ $T_{dry} \in [-40, 0]$ °C, whereas Fig. 7(d) shows the LWC according to our methodology. Farther away from the radar, at around 2.3 km (AMSL), the lidar has already attenuated fully, and thus, the attributed LWC is associated with the radar and/or the radio sounding. The relative significance (90% as opposed to 10%) assigned to each set of observing systems (radar/lidar and radio sounding) is also evident from Fig. 7(d) (compare yellow and red diamonds). Fig. 7(e) and (f) highlights that PIA_λ evaluated by the three-sensor synergy reaches greater
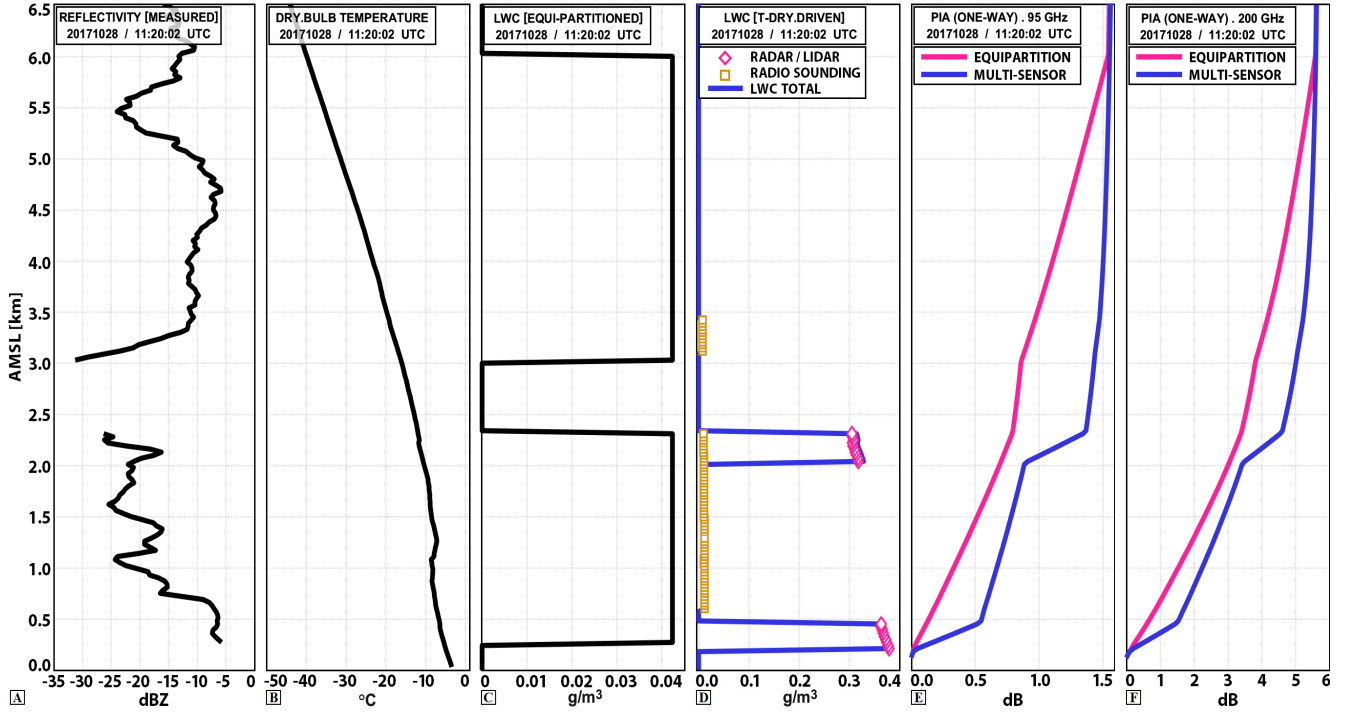
Fig. 7. Vertical profiles of the scene shown in Fig. 3 at 11:20:02 UTC for the fields: (a) radar reflectivity, (b) dry-bulb temperature, (c) equipartitioned LWC for in-cloud, radar-detected data points of $T_{\text{dry}} \in [-40, 0]$ °C as shown in the two leftmost panels, (d) allocated LWC according to the three-sensor methodology in Section IV, (e) one-way PIA at 95 GHz based on the liquid condensate distribution of either (c) or (d), and (f) as in (e) for the G-band operating frequency at 200 GHz.
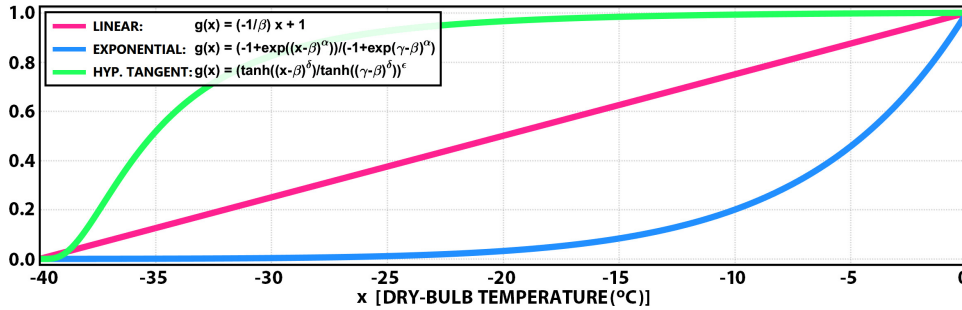

Fig. 8. Monotonically increasing functional forms considered in the T_{dry}-weighted scheme as applied in the current study. Applied structures include (magenta; linear) $g(T) = (-1/\beta)T + 1$, (blue; exponential) $g(T) = (-1 + \exp((T - \beta)^\alpha))/C_{\exp}$, (green; hyperbolic tangent) $(\tanh((T - \beta)^\delta)/C_{\tanh})^\epsilon$, where $C_{\exp} = -1 + \exp((\gamma - \beta)^\alpha)$ and $C_{\tanh} = \tanh((\gamma - \beta)^\delta)$ serve as normalization coefficients for the given set of parameters ($\alpha = 0.62$, $\beta = -40$ °C, $\gamma = 0$ °C, $\delta = 0.4$, and $\epsilon = 15.0$).

values at much lower ranges compared to the attenuation based on the LWC equipartition. Round-trip PIA discrepancies at 95 GHz may be up to 2–3 dB, while at 200 GHz for as high as 5 dB. These values are certainly significantly impacting DWR-based ice cloud-property retrieval methodologies, which demonstrates the relevance of using refined attenuation corrections.

VI. SENSITIVITY ANALYSIS

In our scheme, there are some arbitrary choices in the decision tree of Fig. 1, specifically the selection of the temperature weighting function and the adopted relative weights that partition the attribution of the total LWP to radar/lidar and radio sounding observations, respectively. We briefly evaluate the impact of these assumptions. In addition to the proposed linear temperature weighting, we have considered

two additional temperature weighting schemes based on exponentials and hyperbolic tangents (Fig. 8) and assessed the impact of those functions on the resulting PIAs at both W- and G-band frequencies. For the relative weights between the active sensors and the radio sounding, we have considered an extreme scenario where we allocate 60% of the LWP to the radar/lidar and 40% to the radio soundings. Fig. 9(a) and (b) shows that a maximum 10–15% uncertainty in the PIA profile can be expected depending on the choices for T_{dry} weighting and partial LWP allocation fractions, yet the envelope of our solutions remains clearly distinct from the equipartitioning PIA profiles at both frequencies. The resulting round-trip PIA discrepancy (inclusive of the portrayed spread) across all depicted evaluation instances against the equipartitioning is roughly up to 2 dB at 95 GHz, while at 200 GHz may be significantly larger up to 5 dB.
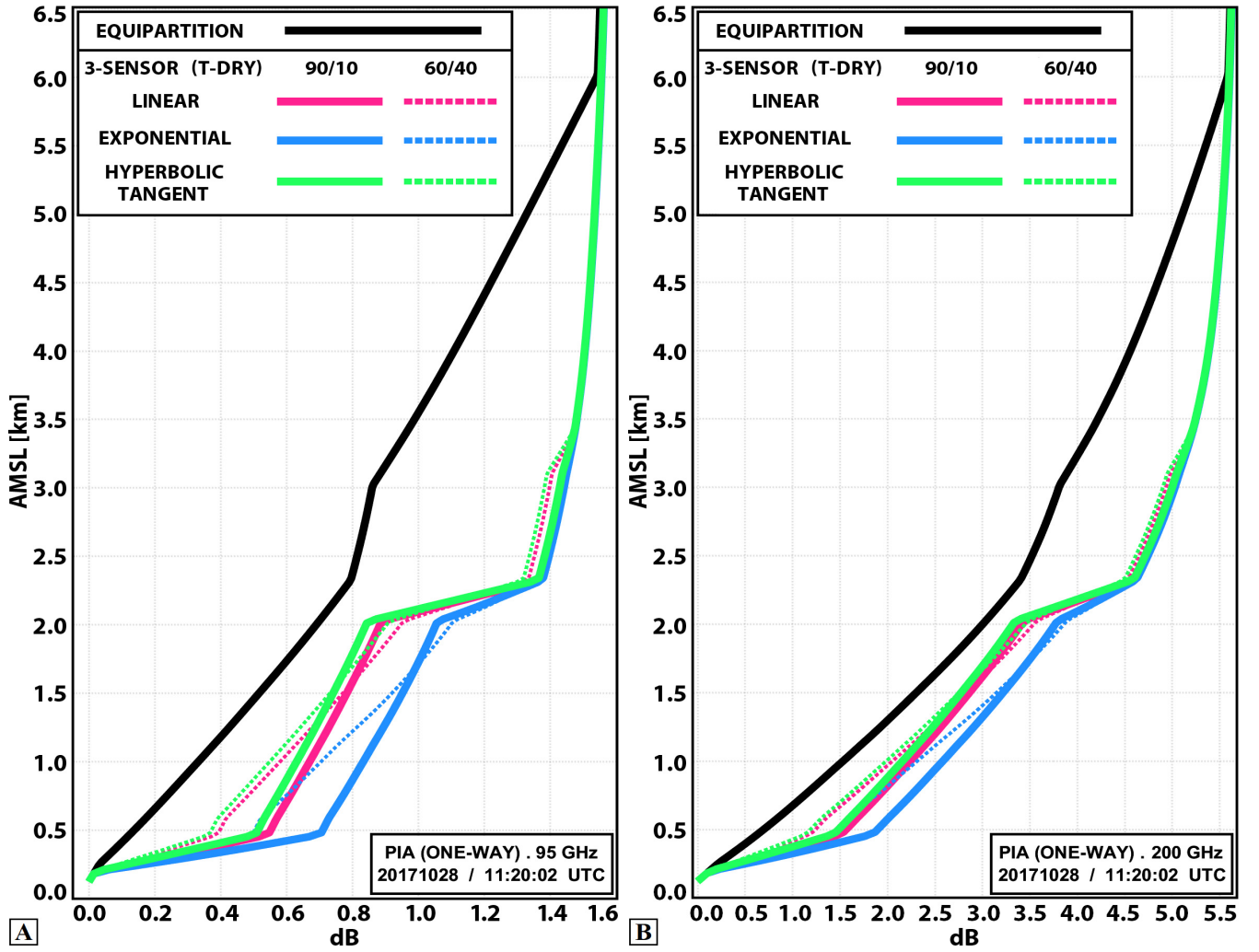
Fig. 9. One-way PIA$_\lambda$ profiles at (a) 95 and (b) 200 GHz of the scene presented in Fig. 3 at 11:20:02 UTC, highlighting the resulting discrepancies across scenarios of LWC vertical distribution evaluated by equipartition (black curve) against the three-sensor synergy applying a T_{dry} weighting of a linear (magenta curve), exponential (blue curve), or hyperbolic tangent (green curve) function for LWP partial allocations set at either (90, 10)% for radar/lidar and S_{liq}, respectively, (solid lines) or (60, 40)% (dashed lines).

Uncertainty pertaining to the MWR-retrieved LWP is conditionally small. The radiometer (NSA.MWR) registers an uncertainty set at 20 g/m^2 irrespective of retrieved LWP amounts. Therefore, for the more critical windows of larger atmospheric moisture aloft (>100 g/m^2), when the treatment of the round-trip attenuation due to liquid water presence is more pressing, the MWR-based ambiguity diminishes substantially. The relative uncertainty in the microwave radiometer LWP retrieval produces an identical relative uncertainty into the PIA product.

VII. DISCUSSION AND CONCLUSION

Multifrequency, radar-based techniques for the microphysical characterization of ice clouds generally require attenuation corrections for estimating the effective reflectivities. Millimeter-radar signal attenuation cannot be neglected, yet it remains challenging given the significant uncertainty of the SLW location, more so when depolarization lidar-based information is not available due to complete lidar extinction from intervening liquid condensate or layers of optically thicker ice.

The current study proposes a three-sensor technique based on radar, lidar, and radio sounding observations for the vertical allocation of the MWR-retrieved LWP, which is deemed more realistic than equipartitioning the LWP within all radar-detected cloudy volumes. Our results show that our SLW distribution produces round-trip PIA profiles that at W- and G-band frequencies, it may significantly depart between the two techniques (with values up to 2 and 5 dB at W- and G-bands, respectively) and that *ad hoc* choices in our methodology have a secondary impact (with maximum discrepancies of the PIA profiles of around 15%).

The proposed methodology has applications within the context of DWR-based, multifrequency ice microphysical retrievals that incorporate W-band or higher frequency radars. For instance, ARM Mobile Facility 2 (AMF2) high-latitude campaigns, such as BAECC [42] or AWARE [43] at Hyytiälä (Finland) and McMurdo Station (Antarctica), respectively, include deployments of W-band cloud radars in multifrequency observational setups inclusive of lidar, radiometer, and radio sounding observations. Similar setups are now available at some CloudNet or cloud physics supersites (e.g., [30], [44]).

Furthermore, attenuation corrections associated with the presence of SLWC in polar environments become imperative for full exploitation of G-band radars and their potential in the microphysical characterization of high-latitude ice and mixed-phase clouds (e.g., [5]).

REFERENCES

[1] P. Kollias *et al.*, "The ARM radar network: At the leading edge of cloud and precipitation observations," *Bull. Amer. Meteorol. Soc.*, vol. 101, no. 5, pp. E588–E607, May 2020, doi: 10.1175/BAMS-D-18-0288.1.

[2] P. Kollias, E. E. Clothiaux, M. A. Miller, B. A. Albrecht, G. L. Stephens, and T. P. Ackerman, "Millimeter-wavelength radars: New frontier in atmospheric cloud and precipitation research," *Bull. Amer. Meteorol. Soc.*, vol. 88, no. 10, pp. 1608–1624, Oct. 2007, doi: 10.1175/BAMS-88-10-1608.

[3] A. Battaglia *et al.*, "Spaceborne cloud and precipitation radars: Status, challenges, and ways forward," *Rev. Geophys.*, vol. 58, no. 3, Sep. 2020, Art. no. e2019RG000686.

[4] R. J. Roy *et al.*, "Boundary-layer water vapor profiling using differential absorption radar," *Atmos. Meas. Techn.*, vol. 11, no. 12, pp. 6511–6523, Dec. 2018.

[5] K. Lamer *et al.*, "Multifrequency radar observations of clouds and precipitation including the G-band," *Atmos. Meas. Techn.*, vol. 14, no. 5, pp. 3615–3629, May 2021. [Online]. Available: https://amt.copernicus.org/articles/14/3615/2021/

[6] A. Battaglia *et al.*, "G band atmospheric radars: New frontiers in cloud physics," *Atmos. Meas. Techn.*, vol. 7, no. 6, pp. 1527–1546, Jun. 2014. [Online]. Available: https://www.atmos-meas-tech.net/7/1527/2014/

[7] K. B. Cooper *et al.*, "G-band radar for humidity and cloud remote sensing," *IEEE Trans. Geosci. Remote Sens.*, vol. 59, no. 2, pp. 1106–1117, Feb. 2021.

[8] M. D. Lebsock, K. Suzuki, L. F. Millán, and P. M. Kalmus, "The feasibility of water vapor sounding of the cloudy boundary layer using a differential absorption radar technique," *Atmos. Meas. Techn.*, vol. 8, no. 9, pp. 3631–3645, Sep. 2015. [Online]. Available: https://amt.copernicus.org/articles/8/3631/2015/

[9] A. Battaglia and P. Kollias, "Evaluation of differential absorption radars in the 183 GHz band for profiling water vapour in ice clouds," *Atmos. Meas. Techn.*, vol. 12, no. 6, pp. 3335–3349, Jun. 2019. [Online]. Available: https://www.atmos-meas-tech.net/12/3335/2019/

[10] R. Roy, M. Lebsock, and M. Kurowski, "Spaceborne differential absorption radar water vapor retrieval capabilities in tropical and subtropical boundary layer cloud regimes," *Atmos. Meas. Techn. Discuss.*, vol. 2021, pp. 1–36, Dec. 2021. [Online]. Available: https://amt.copernicus.org/preprints/amt-2021-111/

[11] R. Lhermitte, "Attenuation and scattering of millimeter wavelength radiation by clouds and precipitation," *J. Atmos. Ocean Technol.*, vol. 7, no. 3, pp. 464–479, 1990. [Online]. Available: https://journals.ametsoc.org/view/journals/atot/7/3/1520-0426_1990_007_0464_aasomw_2_0_co_2.xml, doi: 10.1175/1520-0426(1990)007<0464:AASOMW>2.0.CO;2.

[12] H. Morrison, S. A. Tessendorf, K. Ikeda, and G. Thompson, "Sensitivity of a simulated midlatitude squall line to parameterization of raindrop breakup," *Monthly Weather Rev.*, vol. 140, no. 8, pp. 2437–2460, Aug. 2012, doi: 10.1175/MWR-D-11-00283.1.

[13] A. Battaglia, K. Mroz, D. Watters, and F. Ardhuin, "GPM-derived climatology of attenuation due to clouds and precipitation at Ka-band," *IEEE Trans. Geosci. Remote Sens.*, vol. 58, no. 3, pp. 1812–1820, Mar. 2020.

[14] F. Tridon *et al.*, "The microphysics of stratiform precipitation during OLYMPEX: Compatibility between triple-frequency radar and airborne *in situ* observations," *J. Geophys. Res., Atmos.*, vol. 124, no. 15, pp. 8764–8792, Aug. 2019. [Online]. Available: https://agupubs.onlinelibrary.wiley.com/doi/abs/10.1029/2018JD029858

[15] R. J. Hogan, M. P. Mittermaier, and A. J. Illingworth, "The retrieval of ice water content from radar reflectivity factor and temperature and its use in evaluating a mesoscale model," *J. Appl. Meteorol. Climatol.*, vol. 45, no. 2, pp. 301–317, Feb. 2006, doi: 10.1175/JAM2340.1.

[16] S. Y. Matrosov, A. J. Heymsfield, and Z. Wang, "Dual-frequency radar ratio of nonspherical atmospheric hydrometeors," *Geophys. Res. Lett.*, vol. 32, no. 13, 2005, Art. no. L13816.

[17] S. Kneifel, A. von Lerber, J. Tiira, D. Moisseev, P. Kollias, and J. Leinonen, "Observed relations between snowfall microphysics and triple-frequency radar measurements," *J. Geophys. Res., Atmos.*, vol. 120, no. 12, pp. 6034–6055, Jun. 2015. [Online]. Available: https://agupubs.onlinelibrary.wiley.com/doi/abs/10.1002/2015JD023156

[18] M. Grecu *et al.*, "Nonparametric methodology to estimate precipitating ice from multiple-frequency radar reflectivity observations," *J. Appl. Meteorol. Climatol.*, vol. 57, no. 11, pp. 2605–2622, Nov. 2018, doi: 10.1175/JAMC-D-18-0036.1.

[19] J. Leinonen *et al.*, "Retrieval of snowflake microphysical properties from multifrequency radar observations," *Atmos. Meas. Techn.*, vol. 11, no. 10, pp. 5471–5488, Oct. 2018. [Online]. Available: https://amt.copernicus.org/articles/11/5471/2018/

[20] S. L. Mason, C. J. Chiu, R. J. Hogan, D. Moisseev, and S. Kneifel, "Retrievals of riming and snow density from vertically pointing Doppler radars," *J. Geophys. Res., Atmos.*, vol. 123, no. 24, pp. 13807–13834, Dec. 2018. [Online]. Available: https://agupubs.onlinelibrary.wiley.com/doi/abs/10.1029/2018JD028603

[21] R. J. Chase *et al.*, "Evaluation of triple-frequency radar retrieval of snowfall properties using coincident airborne *in situ* observations during OLYMPEX," *Geophys. Res. Lett.*, vol. 45, no. 11, pp. 5752–5760, Jun. 2018. [Online]. Available: https://agupubs.onlinelibrary.wiley.com/doi/abs/10.1029/2018GL077997

[22] F. Tridon *et al.*, "On the realism of the rain microphysics representation of a squall line in the WRF model. Part I: Evaluation with multifrequency cloud radar Doppler spectra observations," *Monthly Weather Rev.*, vol. 147, no. 8, pp. 2787–2810, Aug. 2019, doi: 10.1175/MWR-D-18-0018.1.

[23] M. Oue, P. Kollias, S. Y. Matrosov, A. Battaglia, and A. V. Ryzhkov, "Combination analysis of multi-wavelength, multi-parameter radar measurements for snowfall," *Atmos. Meas. Techn.*, vol. 2021, pp. 1–33, Mar. 2021. [Online]. Available: https://amt.copernicus.org/preprints/amt-2021-78/

[24] K. Mroz, A. Battaglia, C. Nguyen, A. Heymsfield, A. Protat, and M. Wolde, "Triple-frequency radar retrieval of microphysical properties of snow," *Atmos. Meas. Techn.*, vol. 14, no. 11, pp. 7243–7254, 2021. [Online]. Available: https://amt.copernicus.org/preprints/amt-2021-227/

[25] F. Tridon, A. Battaglia, and S. Kneifel, "Estimating total attenuation using Rayleigh targets at cloud top: Applications in multilayer and mixed-phase clouds observed by ground-based multifrequency radars," *Atmos. Meas. Techn.*, vol. 13, no. 9, pp. 5065–5085, Sep. 2020. [Online]. Available: https://amt.copernicus.org/articles/13/5065/2020/

[26] M. P. Cadeddu, J. C. Liljegren, and D. D. Turner, "The atmospheric radiation measurement (ARM) program network of microwave radiometers: Instrumentation, data, and retrievals," *Atmos. Meas. Tech.*, vol. 6, no. 9, pp. 2359–2372, 2013. [Online]. Available: https://amt.copernicus.org/articles/6/2359/2013/

[27] M. D. Shupe, "A ground-based multisensor cloud phase classifier," *Geophys. Res. Lett.*, vol. 34, no. 22, 2007, Art. no. L22809. [Online]. Available: https://agupubs.onlinelibrary.wiley.com/doi/abs/10.1029/2007GL031008

[28] S. Y. Matrosov and D. D. Turner, "Retrieving mean temperature of atmospheric liquid water layers using microwave radiometer measurements," *J. Atmos. Ocean. Technol.*, vol. 35, no. 5, pp. 1091–1102, May 2018, doi: 10.1175/JTECH-D-17-0179.1.

[29] P. Kalogeras, A. Battaglia, and P. Kollias, "Supercooled liquid water detection capabilities from Ka-band Doppler profiling radars: Moment-based algorithm formulation and assessment," *Remote Sens.*, vol. 13, no. 15, p. 2891, Jul. 2021. [Online]. Available: https://www.mdpi.com/2072-4292/13/15/2891

[30] A. J. Illingworth *et al.*, "CloudNet: Continuous evaluation of cloud profiles in seven operational models using ground-based observations," *Bull. Amer. Meteorol. Soc.*, vol. 88, no. 6, pp. 883–898, 2007.

[31] P. Kollias *et al.*, "Development and applications of arm millimeter-wavelength cloud radars," *Meteorol. Monographs*, vol. 57, pp. 17.1–17.19, Apr. 2016, doi: 10.1175/AMSMONOGRAPHS-D-15-0037.1.

[32] N. Bharadwaj, A. Lindenmaier, K. Widener, K. Johnson, and V. Venkatesh, "Ka-band arm zenith pointing radar network for climate study," in *Proc. 36th Conf. Radar Meteorol.*, 2013. [Online]. Available: https://ams.confex.com/ams/36Radar/webprogram/Paper228620.html

[33] K. Widener, N. Bharadwaj, and K. Johnson, *Ka-Band Arm Zenith Radar (KAZR) Instrument Handbook*. Richland, WA, USA: PNNL, 2012.

[34] E. W. Eloranta, "High spectral resolution LiDAR," in *LiDAR: Range-Resolved Optical Remote Sensing of the Atmosphere* (High Spectral Resolution LiDAR). New York, NY, USA: Springer-Verlag, 2005, ch. 5.

[35] R. J. Doviak and D. S. Zrnič, *Doppler Radar and Weather Observations*, 2nd ed. New York, NY, USA: Academic, 1993, p. 562.

[36] R. M. Rauber and S. W. Nesbitt, *Radar Meteorology: A First Course*, 1st ed. Hoboken, NJ, USA: Wiley, May 2018, p. 488.

[37] H. J. Liebe, "An updated model for millimeter wave propagation in moist air," *Radio Sci.*, vol. 20, no. 5, pp. 1069–1089, 1985. [Online]. Available: https://agupubs.onlinelibrary.wiley.com/doi/abs/10.1029/RS020i005 p01069

[38] A. Protat, S. Rauniyar, J. Delanoë, E. Fontaine, and A. Schwarzenboeck, "W-band (95 GHz) radar attenuation in tropical stratiform ice anvils," *J. Atmos. Ocean. Technol.*, vol. 36, no. 8, pp. 1463–1476, Aug. 2019. [Online]. Available: https://journals.ametsoc.org/view/journals/atot/36/8/jtech-d-18-0154.1.xml

[39] S. G. Cober, G. A. Isaac, A. V. Korolev, and J. W. Strapp, "Assessing cloud-phase conditions," *J. Appl. Meteorol.*, vol. 40, no. 11, pp. 1967–1983, 2001, doi: 10.1175/1520-0450(2001)040<1967:ACPC>2.0.CO;2.

[40] S. G. Cober, G. A. Isaac, and J. W. Strapp, "Characterizations of aircraft icing environments that include supercooled large drops," *J. Appl. Meteorol.*, vol. 40, no. 11, pp. 1984–2002, 2001.

[41] S. G. Cober and G. A. Isaac, "Characterization of aircraft icing environments with supercooled large drops for application to commercial aircraft certification," *J. Appl. Meteorol. Climatol.*, vol. 51, no. 2, pp. 265–284, 2012. [Online]. Available: https://journals.ametsoc.org/view/journals/apme/51/2/jamc-d-11-022.1.xml

[42] T. Petäjä *et al.*, "BAECC: A field campaign to elucidate the impact of biogenic aerosols on clouds and climate," *Bull. Amer. Meteorol. Soc.*, vol. 97, no. 10, pp. 1909–1928, Oct. 2016. [Online]. Available: https://journals.ametsoc.org/view/journals/bams/97/10/bams-d-14-00199.1.xml

[43] D. Lubin *et al.*, "AWARE: The atmospheric radiation measurement (ARM) west Antarctic radiation experiment," *Bull. Amer. Meteorol. Soc.*, vol. 101, no. 7, pp. E1069–E1091, Jul. 2020, doi: 10.1175/BAMS-D-18-0278.1.

[44] J. D. Neto *et al.*, "The triple-frequency and polarimetric radar experiment for improving process observations of winter precipitation," *Earth Syst. Sci. Data*, vol. 11, no. 2, pp. 845–863, Jun. 2019. [Online]. Available: https://essd.copernicus.org/articles/11/845/2019/

Petros Kalogeras received the M.Sc. degree in computational physics from the Aristotle University of Thessaloniki, Thessaloniki, Greece, in 2010, and the M.Sc. degree in meteorology from Pennsylvania State University, State College, PA, USA, in 2015. He is currently pursuing the Ph.D. degree with the Department of Physics and Astronomy, University of Leicester, Leicester, U.K.

He has been a private tutor, a teaching assistant, and a laboratory demonstrator. Earlier research interests included subject matters in dynamic meteorology, weather systems, and data assimilation. Contemporary research is focused on ice microphysics and high-latitude processes, based on cloud monitoring from a suite of active and passive remote sensing instruments within the multiwavelength observational context.

Alessandro Battaglia graduated from the University of Padova, Padua, Italy, with a thesis in particle physics. He received the Ph.D. degree in physics from the University of Ferrara, Ferrara, Italy, in 2001.

He is experienced in microwave remote sensing of clouds and precipitation with a specific interest in spaceborne radars. Currently, he has a joint appointment as an Associate Professor at the Department of Physics, University of Leicester, Leicester, U.K., and the Dipartimento di Ingegneria dell'Ambiente, del Territorio e delle Infrastrutture (DIATI), Politecnico di Torino, Turin, Italy. He has extensive experience in active and passive microwave modeling. He has developed radar forward modeling capable of simulating Doppler spaceborne radars. He has worked on polarization diversity and developed retrieval algorithms for multifrequency observations. He is a member of the NASA Precipitation Measuring Mission Science Team, the ESA MAG of EarthCARE, and U.K.-NCEO. He has authored or coauthored more than 80 peer-reviewed journal articles.